RESEARCH ARTICLE

Natural Sciences

Design strategies of the mantis shrimp spike: How the crustacean cuticle became a remarkable biological harpoon

Yann Delaunois[1] | Alexandra Tits[2] | Quentin Grossman[2] | Sarah Smeets[1] | Cédric Malherbe[3] | Gauthier Eppe[3] | G. Harry van Lenthe[4] | Davide Ruffoni[2] | Philippe Compère[1,5]

[1]Laboratory of Functional and Evolutionary Morphology, FOCUS Research Unit, Department of Biology, Ecology and Evolution, University of Liège, Liège, Belgium

[2]Mechanics of Biological and Bioinspired Materials Laboratory, Department of Aerospace and Mechanical Engineering, University of Liège, Liège, Belgium

[3]Mass Spectrometry Laboratory, MolSys Research Unit, Department of Chemistry, University of Liège, Liège, Belgium

[4]Department of Mechanical Engineering, KU Leuven, Leuven, Belgium

[5]Center for Applied Research and Education in Microscopy (CAREM) and Biomaterials Interfaculty Center (CEIB), University of Liège, Liège, Belgium

Correspondence
Davide Ruffoni, Mechanics of Biological and Bioinspired Materials Laboratory, Department of Aerospace and Mechanical Engineering, University of Liège, Quartier Polytech 1, Allée de la Découverte 9, B-4000 Liège, Belgium.
Email: druffoni@uliege.be

Philippe Compère, Laboratory of Functional and Evolutionary Morphology, Department of Biology, Ecology and Evolution, University of Liège, Quartier Agora, Allée du six Août 15, B-4000 Liège, Belgium.
Email: pcompere@uliege.be

Davide Ruffoni and Philippe Compère equal supervision of the work and corresponding authors.

Funding information
FRIA Doctoral Grant (Fund for Research Training in Industry and Agriculture of the F.R.S.-FNRS), Grant/Award Numbers: 5202920F, 5129219F; Centre for Applied Research and Education in Microscopy (CAREM, ULiege)

Abstract

Spearing mantis shrimps are aggressive crustaceans using specialized appendages with sharp spikes to capture fishes with fast movement. Each spike is a biological tool that has to combine high toughness, as required by the initial impact with the victim, with high stiffness and strength, to ensure sufficient penetration while avoid breaking. We performed a multimodal analysis to uncover the design strategies of this harpoon based on chitin. We found that the spike is a slightly hooked hollow beam with the outer surface decorated by serrations and grooves to enhance cutting and interlocking. The cuticle of the spike resembles a multilayer composite: An outer heavily mineralized, stiff, and hard region (with average indentation modulus and hardness of 68 and 3 GPa), providing high resistance to contact stresses, is combined with a less mineralized region, which occupies a large fraction of the cuticle (up to 50%) and features parallel fibers oriented longitudinally, enhancing stiffness and strength. A central finding of our work is the presence of a tiny interphase (less than 10 μm in width) based on helical fibers and showing a spatial modulation in mechanical properties, which has the critical task to integrate the stiff but brittle outer layer with the more compliant highly anisotropic parallel-fiber region. We highlighted the remarkable ability of this helicoidal region to stop nanoindentation-induced cracks. Using three-dimensional multimaterial printing to prototype spike-inspired composites, we showed how the observed construction principles can not only hamper damage propagation between highly dissimilar layers (resulting in composites with the helical interphase absorbing 50% more energy than without it) but can also enhance resistance to puncture (25%

increase in the force required to penetrate the composites with a blunt tool). Such findings may provide guidelines to design lightweight harpoons relying on environmentally friendly and recyclable building blocks.

KEYWORDS
biocomposite, crustacean, harpoon, high stiffness and toughness, stomatopod, spike, multilayer, multimodal analysis

Key Points

– The heavily mineralized biological appendages of the mantis shrimp are a constant source of inspiration for developing new engineering materials.
– We use characterization methods of material science to investigate a biological harpoon based on chitin.
– Several morphological, compositional, microstructural, and biomechanical features are highlighted, allowing the spikes of the mantis shrimp to be remarkable lightweight, tough, and stiff harpoons.

INTRODUCTION

The arthropod cuticle is one of the most remarkable and versatile biological material.[1] Not only does it provide protection to all body parts, but it also forms highly sophisticated appendices, dedicated to specific functions. The cuticle enables basic tasks, such as physiological exchanges, sensing and actuation,[2–4] walking, climbing and adhesion on different surfaces,[5] swimming, and flying.[6] Food treatment (e.g., through mandibles and stomach teeth),[7] mechanical[8,9] and optical shielding,[10] as well as puncturing and capturing[11] are additional ingenious functions performed with the cuticle. It is remarkable that such multifunctionality is obtained thanks to a tiny and lightweight biological structure, formed by the epidermis, renewed periodically by the molting process, and essentially comprising a thin superficial waterproof layer (the epicuticle) made of a lipid-protein matrix, and a thicker internal fibrous layer (the procuticle), generally subdivided into exo- and endocuticle depending on secretion time.[12,13] The basic building blocks of the procuticle are the chitin–protein microfibers, composed of a crystalline α-chitin core, which is coated by a helical sheath of protein units.[14–17] Matrix proteins are also found outside the microfibers when considering higher structural organization. The chitin–protein microfibers interact with a (partially) proteinaceous and hydrated matrix, which features a rich variety of proteins, enabling selective cross-linking.[17–19] The relative fraction of protein and matrix is not well known for the mantis shrimp and may depend on the considered region. Previous data on decalcified crab cuticles indicate that chitin content should range between 50% and 75% dry weight.[20] In areas of the cuticle where hardness and wear resistance are major requirements, the chitin–protein biocomposite is reinforced either by mineral incorporation in the matrix or by sclerotization that cross-link the matrix, sometimes with the help of transition metals (e.g., Mn, Zn,

and Fe) as seen in insect mandibles[21] and spider fangs.[22] In the procuticle, the chitin–protein microfibers assemble in larger bundles to form fibers, and, in turn, the fibers form higher order structural motifs: Arrays of locally aligned fibers are assembled into beds, and several beds are stacked into a three-dimensional helicoidal twisted plywood structure, resembling a man-made laminate, but at the nano/micro length scales.[23,24] The regular rotation of the fibers in horizontal beds gives rise to a periodic lamellate aspect, each lamella corresponding to a rotation of 180°. The composition of the matrix, the type of sclerotization, and the relative fraction of reinforcing minerals, together with the tunable fiber organization and lamellar thickness, are at the bases of the outstanding versatility of the arthropod cuticle, and, consequently, they are key elements of the evolutionary success of arthropods in a variety of very dissimilar environments.[24,25]

An instructive example of how the cuticle has evolved into highly specialized tools, even within the same organism, is found in the stomatopod crustaceans (or mantis shrimps). During their evolution, these marine animals modified their cuticle for feeding, hunting, and defense purposes.[9] Stomatopods are traditionally subdivided into two branches based on the structure of their anterior appendages[26–28]: the well-known "smashers" that use a hammer-like club to destroy hard-shell preys, and the less famous "spearers" (Figure 1a) that have a harpoon-like appendage to impale and grasp their (generally) soft-body preys. Thanks to an efficient "amplification system," which includes a dedicated area (the saddle) to store and release elastic energy,[29] together with an ingenious system of articulation,[30] stomatopods can deploy their anterior appendages at impressive velocities (up to 6 m/s for the spearers and to 23 m/s for the smashers).[31] Repetitive impacts at such velocities require excellent damage tolerance, and previous investigations have revealed that the hammer-club of the smashers shows numerous strategies to cope with damage.[28,32–34]
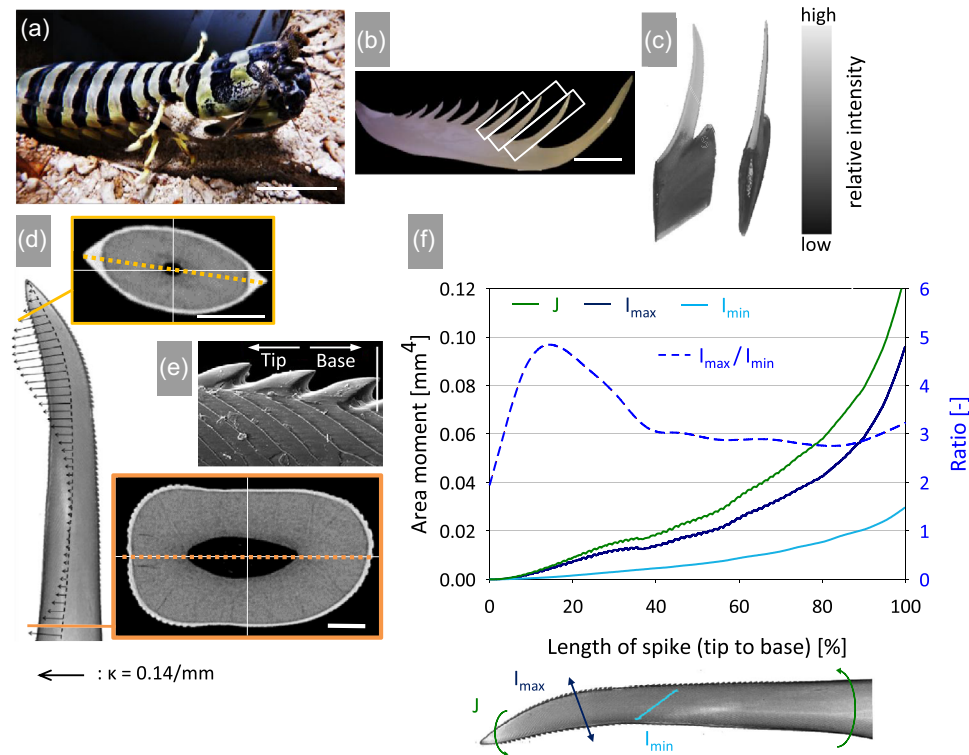
FIGURE 1 Morphology and biomechanics of the spike from the spearing mantis shrimp *Lysiosquillina maculata*: (a) photograph of a specimen (scale bar: 5 cm) and (b) of a raptorial appendage showing, in the white boxes, the distal spikes characterized here (scale bar: 1 cm); (c) micro-computed tomography (Micro-CT) reconstruction of a distal spike attached to the dactyl. The grey level gives a qualitative indication of the heterogeneous density of the cuticle (increasing density from dark to light grey); (d) micro-CT reconstruction of a single spike showing the gross morphology. Superimposed to the micro-CT are arrows having length proportional to the local curvature κ of the spike (a representative arrow indicating a curvature of 0.14 mm^{-1} is shown at the bottom). The insets (yellow and orange boxes) show two typical cross sections at the base and near the tip of the spike (scale bars: 200 μm). By comparing the two cross sections, a slight rotation (of about 15°) along the main axis of the spike is evident; (e) side view of the lateral outer border of the spike in SE-scanning electron microscopy (SEM) showing serrations and surface grooves; (f) spatial variations of maximum (I_{max}) and minimum (I_{min}) second area moments as well as polar moment (J) of the spike cross sections along the spike's length.

Macroscopically, the size of the club is smaller than the critical radius at which, according to contact mechanics, the damage response switches from quasi-plastic to brittle, thus hampering catastrophic failure.[33] Microscopically, the club presents three different regions solving different mechanical functions: a heavily mineralized impact region characterized by mineral gradients[32,35] and by oriented fluorapatite (FAP) crystals perpendicular to the outer surface to enhance impact resistance; beneath the impact region there is a less mineralized periodic region showing the common helicoidal twisted plywood pattern, which may dissipate possible cracks generated during impact[32]; on the lateral sides, the periodic region is encircled by a striated region with chitin fibers well aligned along a preferential orientation.[32] This belt-like area is believed to provide later confinement to the periodic region, hence preventing high tensile stresses and the associated tensile cracking.[28]

Although deployed at smaller velocities, the anterior appendage of the spearer is not less fascinating. It is a biological tool solving multiple functions: Its base presents a flat surface used to hammer the opponents and sharing some of the construction strategies seen in the smasher.[28,35] On the top, it is decorated by several spikes

(Figure 1b) that, in analogy to man-made harpoons, have to penetrate and grab preys within a fraction of second during a high-speed capturing event.[31] This task requires the combination of conflicting mechanical requirements: Not only the spike must be tough to cope with the initial impact with the victim but also stiff to avoid large deflections while penetrating a moving target, and it must be strong to prevent rupture and prey loss. These constraints should come together with additional strategies to retain the prey. By comparing the spike cuticle of spearing limbs with different body parts (i.e., cephalic shield and abdominal tergites), we revealed some compositional and microstructural modifications of the cuticle in the spike. These include (i) the replacement of the leathery inner epicuticle (commonly having an organic nature) by a highly mineralized exocuticle reinforced by FAP and (ii) the development of a unidirectional fiber region interrupting the classical helicoidal twisted plywood structure in the less mineralized endocuticle.[36] Here, we investigate the spike in more details and at multiple length scales using micro-computed tomography (micro-CT), backscattered and secondary electron imaging based on scanning electron microscopy (BSE–SEM and SE-SEM), elemental analysis by energy-dispersive spectroscopy (EDS), confocal Raman spectroscopy,

depth sensing nanoindentation, and multimaterial 3D printing. The central aim of our work is to elucidate the structure–function relationship and the mechanical behavior of the spike, highlighting the morphological, compositional, and microstructural adaptations allowing this biological tool, which is built very quickly, to be an effective natural harpoon.

RESULTS AND DISCUSSION

Morphology and biomechanics of the entire spike

The raptorial appendage of the spearer zebra mantis shrimp *Lysiosquillina maculata* (Figure 1a) features 10 spikes of increasing size, regularly arranged along the dactyl (Figure 1b). The morphology and the external surface of distal spikes were characterized by high-resolution micro-CT and SEM. Each distal spike is a tapered, thin, and elongated offensive weapon (Figure 1c). In contrast to the straight needlelike shape common to many man-made harpoons,[11] it has a curved form and an elliptical cross section (Figure 1d). The local curvature of the spike varies along its length such that three regions can be identified: a slightly curved zone close to the base, a fairly straight segment in the middle, and a region with the highest curvature before reaching the tip (Figure 1d, the length of the arrows is proportional to the local curvature $\varkappa$). This allows the spike to orient its sharp end at an almost right angle with respect to the dactyl within a short distance while avoiding a large angle at the base, which may cause stress localization upon bending. A curved rather than a straight profile may be linked to the curved trajectory of the appendage during a strike[31] and could as well facilitate the parking of the spikes within dedicated holes in the propodus at resting position (Figure S1). In nature, the shape of puncturing systems is highly diverse and closely connected with their function.[11] A straight offensive tool such as the harpoon of the cone snail,[37] the bee stinger,[38] or the mosquito proboscis[39] may be used to maximize penetration depth,[11] whereas highly curved devices like crustaceans claws[40] or spider fangs[41] should enable puncture along different trajectories and facilitate prey retention.[35,37] The unusual form of the spike, featuring both curved and straight zones, may be a trade-off between large penetration depth and prey grabbing. Micro-CT imaging of spike cross sections reveals a thin highly mineralized cover bordering a less mineralized but much thicker layer with a central cavity (Figure 1d). This dual mineralization is a specific reinforcement feature of raptorial appendages used for impaling or smashing preys as well as for fighting with opponents.[28,32,34–36] In general, the electron-dense region is particularly pronounced on the impact surface and much less in other parts of the cuticle.[9,42] After a heavily mineralized and sharp tip, characterized by a radius of curvature of about 20 μm, which should facilitate puncture into the tough skin of the preys, the spike exhibits a spatially varying geometry. The cross sections have an ellipsoidal profile, and the cross-sectional area increases gradually from the tip to the base, always having a pronounced eccentricity (Figure S2). An additional peculiarity is a small rotation (of about 15°) of the cross section around the longitudinal axis of the spike (insert in Figure 1d), resulting in a

slightly twisted shape. From a biomechanical viewpoint, such a slender and ellipsoidal hollow beam may suffer from low bending and torsional rigidity, thus questioning the ability to remain straight during a capturing event. We evaluate how cross-sectional properties evolve along the longitudinal length of the spike and we estimate the consequences for bending and torsional resistance using second area and polar moments as surrogates for mechanical properties (Figure 1f). Both maximum and minimum second moments of area (I_{max} and I_{min}), corresponding approximately to dorsoventral and lateral loadings, increase proximally and show a steeper slope starting at ~90% of the spike length, where the spike begins to merge with the appendage. The polar moment J (a proxy for torsional rigidity) follows a similar trend, being bound by I_{min} and I_{max}. Despite a fairly high eccentricity, the ratio I_{max}/I_{min} suggests only a moderate mechanical anisotropy, with resistance to dorsoventral loading (i.e., parallel to the prevalent hunting movement of the raptorial appendage) being in average 3.3 times higher than lateral loading. Additionally, the ratio I_{max}/I_{min} is fairly constant for about 60% of the spike length. Although simplified, this analysis suggests that the spike is not only very stiff along the longitudinal direction but it can also face multiaxial loading, consistent with the assumed ability of the spearing mantis shrimps to control and direct the strike.[31]

The outer surface of the spike is decorated with two reinforcing serrated ridges, running all the way from the tip to the base (Figure 1e). Such "shark fin-shaped" serrations are part of the highly mineralized layer; with the exception of a zone close to the tip, they have fairly constant dimensions (i.e., ~100 μm in height and ~55 μm in length, Figure S3) in the first third of the spike, whereas their size decreases when approaching the base, suggesting that only a portion of the spike (closer to the tip) is engaged to impale the preys. Serrations are prominent features in many diverse biological cutting tools, ranging from teeth to insect stingers,[43] and could have a dual function: They should help to cut through the tissue of the prey by acting as local stress concentrators and, owing to their specific shape, they may prevent the prey from slipping off the spikes by interlocking with the damaged tissue.[11] In addition to the serrations, the surface of the spikes features a characteristic "grooved" pattern (Figure 1e and Figure S3). The grooves have a periodic spiral arrangement, starting and ending at two opposite serrated ridges, and have dimensions smaller than the serrations (i.e., ~5 μm in height and ~35 μm in width, Figure S3). The grooves should provide the spike surface with a controlled roughness, which may increase frictional forces as an additional strategy, at a smaller length scale, to enhance prey retention. From a biological viewpoint, grooves should reflect the specific growth pattern of the spike outer layer, regulated by the epidermis cells that are arranged into parallel arrays.

Microstructure

The microstructure of the spike, observed with SEM on fractured and polished samples, features four regions with distinct fiber architecture (Figure 2a,b and summary scheme in (I)). The first innermost layer, named inner helicoidal region (IHR, Figure 2c), belongs to the
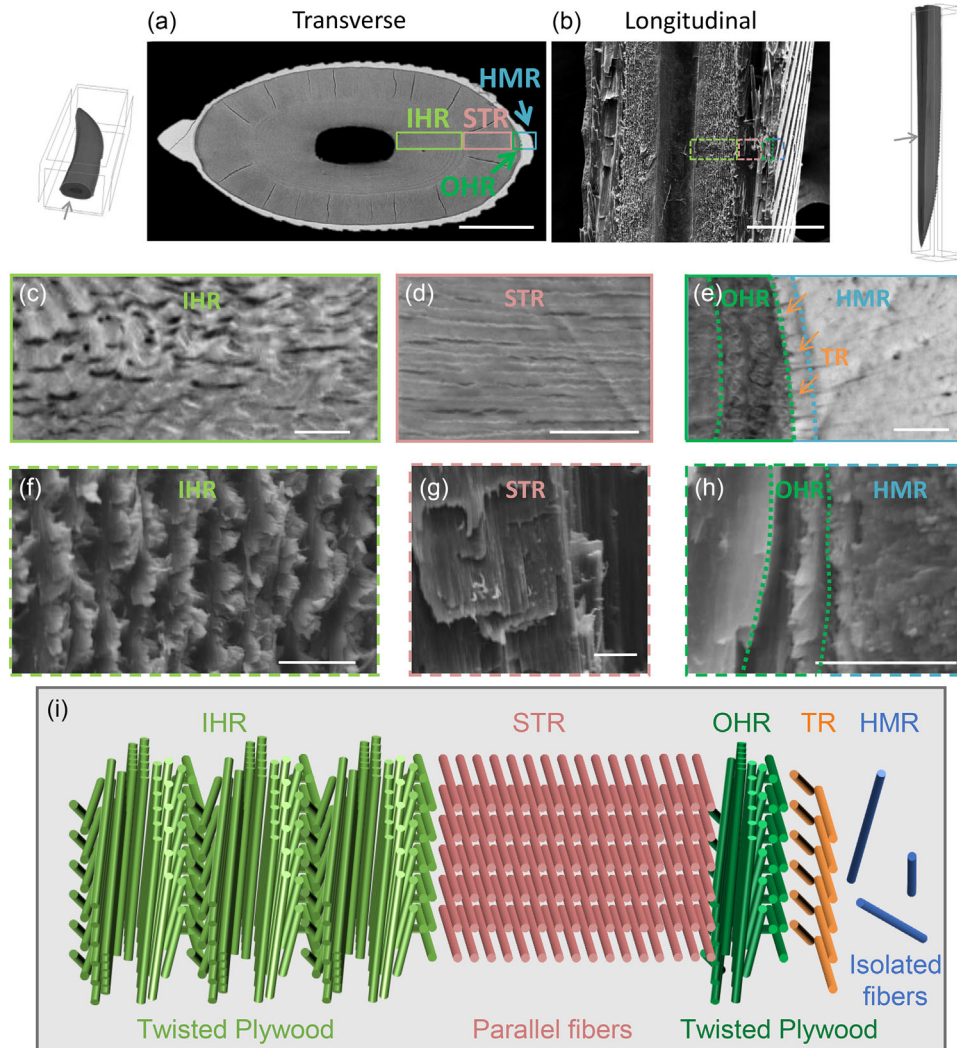
FIGURE 2 Microstructure of the spike: (a) representative polished transversal section imaged in backscattered electron–scanning electron microscopy (BSE–SEM) accompanied on the left by a micro-computed tomography (micro-CT) reconstruction showing the location of the cross section. The multilayered architecture of the cuticle, comprising a highly mineralized region (HMR), an outer helicoidal region (OHR), a striated region (STR), and an inner helicoidal region (IHR) is evident; (b) SE-SEM of a longitudinal fracture offering a complementary view of the four layers accompanied, on the right, by a micro-CT reconstruction showing the location of the cross section. Scale bars in (a) and (b) are 200 μm; (c–e) details of the different layers from the polished surface. In part (e), the arrows indicate the transition region (TR) and the dotted lines bound the OHR. In part (d), horizontal parallel chitin–protein fibers are cross-sectioned, and fiber-rich strands (medium dark) alternate with pore canal lumens (dark), and their densely mineralized sheaths (bright rodlike features). Twisted ribbon-shaped pore canals with unmineralized lumen also appear in the IHR (c) and in the OHR (e), whereas they are straight and mineralized in the HMR (e). Scale bars in (c–e): 10 μm. (f–h) Close-up views of the fractured surface of the different layers highlighting: (f) a rough surface for the IHR in agreement with the twisted plywood organization; (g) sheets of parallel fibers (oriented vertically in the figure) in the STR and (h) a rough stepwise fractured surface in connection with the OHR (bounded by dotted lines), which is in strike contrast with the smoother surface of the HMR; (i) schematic summarizing the main microstructural features of the spike. Scale bars in (f–h): 8 μm.

endocuticle[36] and displays a twisted plywood organization consisting of numerous lamellae gradually increasing in thickness from about 1.5 to 10 μm when moving outward. Within each lamella, layered beds of chitin–protein fibers embedded into a protein–mineral matrix are stacked with regular changes in fiber directions between each bed, resulting in stepwise and rough fracture surfaces (Figure 2f). Pore canals, pervading the cuticle up to the epicuticle, are visible at high magnification SEM and have a characteristic twisted-ribbon shape[44]

with unmineralized dark lumens (Figure 2c). They serve for the secretion of the cuticle and perhaps provide supplementary "waterproof" capability, as inferred by their lipid content.[36] In the second layer, referred as the striated region of the endocuticle (STR), the helicoidal pattern is replaced by highly aligned fibers parallel to the long axis of the spike as highlighted by a longitudinally fractured sample showing fiber sheets (oriented vertically in Figure 2g). In this region, the pore canals lose their typical twisted-ribbon aspect and cross

perpendicularly to the horizontal fiber beds, giving a characteristic striated pattern typically observed in polished (transverse) sections, where the canal lumen appears dark, and the mineralized fibrous sheath appears bright (Figure 2d). Although the twisted plywood motif is universal in the arthropod cuticle, the parallel-fiber organization is very unusual.[22] In stomatopods, striated regions with parallel longitudinal fibers have been found only in specific locations, including the dactyl club of the smasher,[32] the impact area of the dactyl in the appendage carrying the spikes of the spearer,[28] and the back defensive spikes located at the uropods (posterior structures found in crustaceans).[42] One common feature of those locations is a challenging biomechanical environment, solving critical offensive or defensive tasks. Most interestingly, sandwiched between the striated and the external region, there is an additional layer of the endocuticle[36] presenting a twisted plywood organization (Figure 2e), called outer helicoidal region (OHR). This location has two unusual features: It is composed of a very limited number of lamellae, spanning a width of only a few micrometers, and it appears darker under BSE imaging, indicating a lower mineral content. Even more, when going from this OHR to the exterior of the spike exocuticle, the helicoidal architecture is not lost immediately, but there is a transition region (TR) having high mineral content (arrows in Figure 2e) and characterized by one interface lamella. The last region of the spike cuticle identified here is the external highly mineralized region (HMR), where larger and more isolated fibers achieve a last half rotation within a heavily mineralized matrix before the twisted plywood organization is finally lost toward the spike outer surface.[36] The presence of a continuous twisted plywood at the interface between the HMR and the less mineralized OHR is a remarkable feature of the spike that may enhance the anchoring between such dissimilar layers, as suggested by the rough fracture surface at that location (Figure 2h). A closer examination of fracture surfaces (Figure S4) highlights that in this HMR, crystals form nanometer-sized crystallites, in analogy with those found in the dactyl club's outer layer.[35] The remaining of the HMR presents a very low fraction of chitin–protein fibers,[36] but it is still traveled by numerous pore canals, running perpendicular to the interface with the OHR (Figure 2e). The spike cross section is largely dominated by the striated and by the IHRs: For about two third of the spike length, 90% of the wall thickness is only due to those two regions with the contribution of the OHR and of the HMR being about 3% and 7%, respectively (Figure S5).

Composition

The spike has a spatially tuned and graded chemical composition featuring three different minerals: FAP, amorphous calcium phosphate (ACP), and amorphous calcium carbonate (ACC). The minerals are closely related to the underlying microstructural organization and fiber architecture. Elemental microanalysis by EDS on representative locations highlights the presence of C, O, P, and Ca as major chemical elements and of F, Na, and Mg as minor components.[36] Those elements are unevenly distributed in the different regions as shown on a transverse cross section (Figure 3a) using 2D elemental mapping

(Figure 3b–d), and line scans (Figure 3e,f and Figure S6). The HMR is rich in Ca and P together with F; a complementary Raman analysis, focusing on the outer part of the spike cuticle (Figure 4a), shows a fairly sharp phosphate peak centered at 965 cm^{-1} (Figure 4b), indicating that FAP is most likely the predominant mineral phase of this region.[7,45] The sharpness of the peak further suggests a high degree of crystallinity.[35] Confocal Raman imaging reveals interesting spatial heterogeneities within the HMR. First, the phosphate band presents higher intensity at the outer surface as well as in the TR close to the individual lamella anchoring the HMR to the less mineralized thin OHR (arrows in Figure 4c). This agrees with variations in P concentration detected by EDS (Figure 3e). The same zone co-localizes with an increased crystallinity of FAP, estimated by the full width at half maximum (FWHM) of the phosphate peak (Figure 4d). One additional feature of the HMR is a central band having relatively low phosphate intensity and crystallinity, along with some traces of ACC (arrows in Figure 4f). Comparison of the phosphate intensity at the 0° and 90° polarization angles confirms spatial differences in the orientation of the mineral phase, with less oriented minerals found in regions with higher FWHM (Figure 4e and Figure S7). A similar tuning of the mineral phases has been reported at the impact region of the spearing dactyl, with small amounts of sulfate co-localized with the more crystalline FAP regions.[35] The presence of FAP, rather than the more common ACP, is a remarkable compositional modification at the surface of spearing and smashing appendages of the mantis shrimp.[35] In decapods crustaceans, a similar modification involving FAP occurs in the external layer covering the molar area of the crayfish mandible.[7] This mineral is used not only to enhance the biomechanical performance of the cuticle, providing superior impact and wear resistance, but the presence of fluor decreases the solubility of apatite, thus improving its chemical stability. At the interface between the highly mineralized and the OHRs, there is an abrupt transition in the mineral from FAP to ACP as indicated by the sudden shift in phosphate position (Figure 4g). A central observation of the compositional analysis performed here is that the thin OHR has the lowest mineral content as inferred by Ca and P concentrations both showing a minimum there (Figure 3e). Moving further toward the interior of the spike, ACP still predominates within the striated region, whereas in the IHR, it is gradually replaced by Mg-rich ACC.[36]

Nanoscopic biomechanical properties: indentation modulus, hardness, and damage behavior

The region-dependent chemical composition and microstructural organization of the spike cuticle are reflected into spatially varying mechanical properties, as measured by depth sensing nanoindentation (Figure 5a). The outer FAP-dominated region is clearly the stiffest and hardest location (indentation modulus of 64.9 ± 3.5 GPa and hardness of 4.0 ± 1.0 GPa). Both mechanical parameters show a considerable drop (almost a factor of 2 for the modulus and of 5 for hardness) in the thin OHR, which displays the lowest values of the entire spike, consistent with the low mineral content and compositional modifications. Moving to the striated region, indentation modulus and hardness
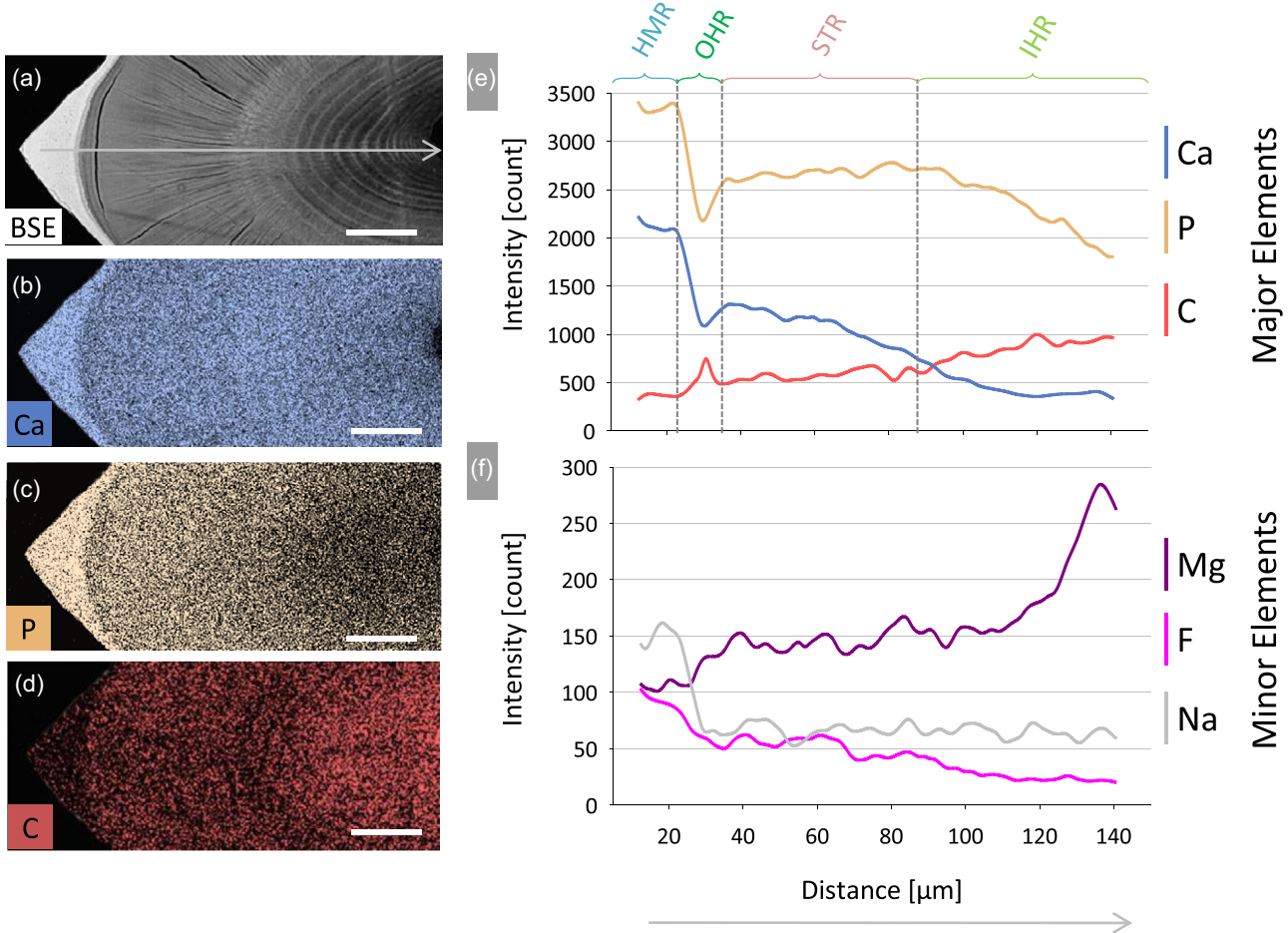
FIGURE 3 Energy-dispersive spectroscopy (EDS) elemental mappings and profiles (line scans) on (a) backscattered electron–scanning electron microscopy (BSE–SEM) image of a polished cross section of the spike cuticle. The dotted line represents the location where the profile plots in (e) and (f) were taken; (b–d) elemental mapping of (b) calcium, (c) phosphorus, and (d) carbon; line scans of selected (e) major and (f) minor elements along the dotted line in (a) from the outer surface toward the inner epidermis. HMR, highly mineralized region; IHR, inner helical region; OHR, outer helical region; STR, striated region. Scale bars: 50 μm.

TABLE 1 Local mechanical properties (indentation modulus E, and hardness H) of the different regions of the spike cuticle measured with nanoindentation using a cube corner probe

Region	E (GPa)	H (GPa)
HMR	68.33 ± 5.05	2.96 ± 0.39
TR	42.35 ± 4.88	1.51 ± 0.23
OHR	21.13 ± 3.49	0.62 ± 0.16
STR	32.46 ± 3.87	0.85 ± 0.08
IHR	31.00 ± 3.18	0.85 ± 0.09

Note: Values are reported as mean ± standard deviation.
Abbreviations: HMR, highly mineralized region; IHR, inner helicoidal region; OHR, outer helical region; STR, striated region; TR: transition region.

increase, and the former also shows slightly higher values with respect to the inner twisted plywood (Table 1), which is conceivable considering the highly ordered arrangement of the fibers. Furthermore, a small negative gradient of about 4 GPa is observed in the indentation modulus in this location, probably reflecting the corresponding decrease in

Ca content. To better characterize the spatial tuning in local mechanical behavior from the heavily mineralized to the parallel-fiber region, we performed high-resolution nanoindentation with a sharp cube corner probe (Figure 5b–e and Figure S8). The high-resolution maps confirm the unusual drop in modulus within the outer twisted plywood region, with values slightly below 20 GPa and no differences between longitudinal and transverse sections, consistent with the isotropic nature of the twisted plywood organization. In particular, the TR (featuring an individual lamella with fairly high mineral content) has a clear signature in the mechanical maps (Figure 5d,e) with a modulus of about 40–45 GPa, allowing a gradual switch from the highly mineralized to the OHR. One additional feature of the HMR is a quite heterogeneous mechanical behavior (Figure S9), likely reflecting the spatial variations of phosphate intensity and crystallinity measured by the Raman spectroscopy. A similar mechanical modulation featuring stiffer crystalline domains and less stiff amorphous islands has been reported for the heavily mineralized impact region of the spearer appendage.[35] Although a thin OHR enclosing highly co-aligned fibers has been found in other biological penetrating tools such as the uropod back spike of
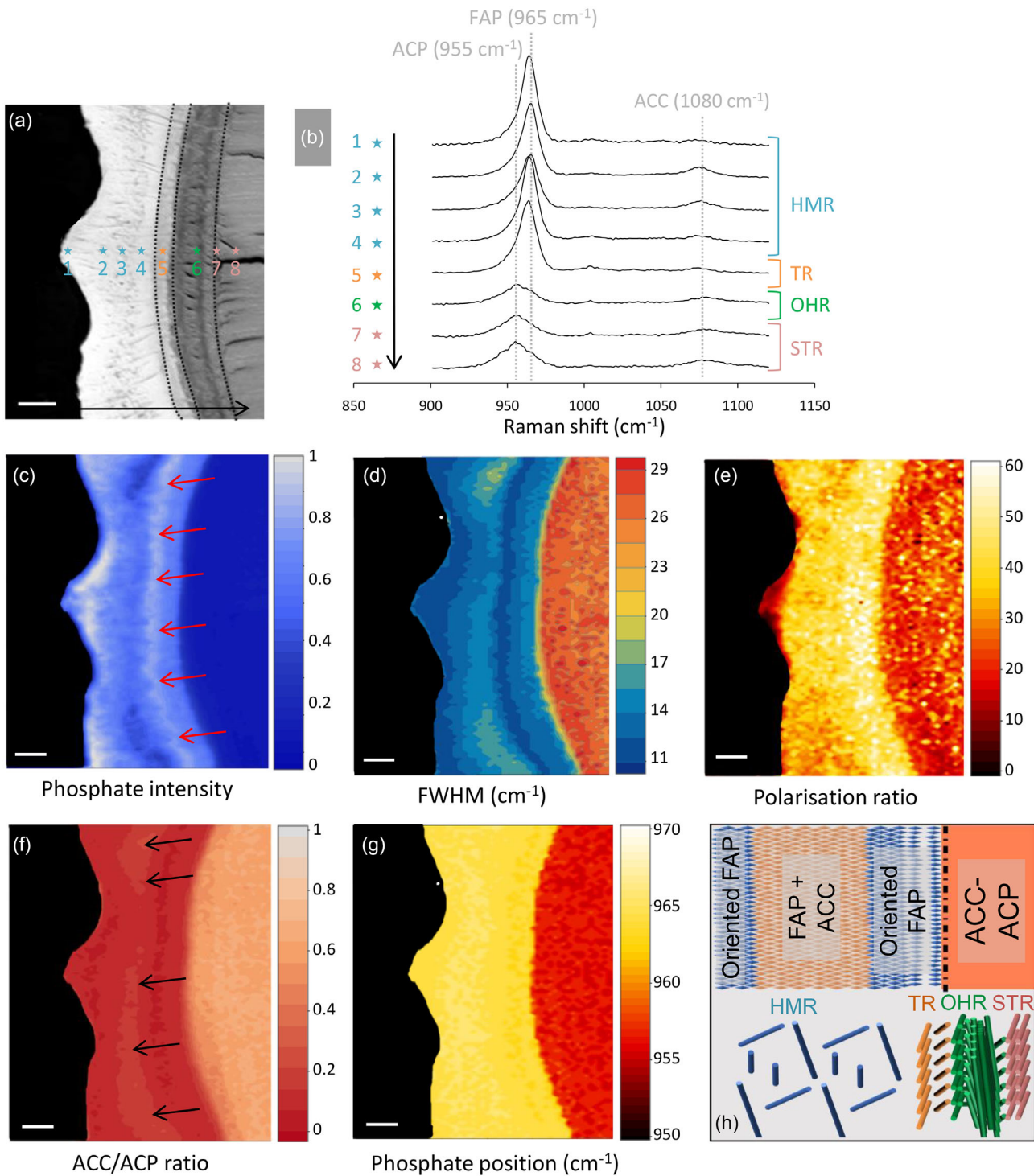
FIGURE 4 Raman spectroscopy of the outer regions of the spike cuticle: (a) backscattered electron–scanning electron microscopy (BSE–SEM) image highlighting the locations of the Raman spectra and mapping (scale bar: 10μm); (b) the Raman spectra obtained in different locations across a straight line from the heavily mineralized outer surface to the striated region. Three different peaks corresponding to amorphous calcium phosphate (ACP, 955 cm^{-1}), fluorapatite (FAP, 965 cm^{-1}), and amorphous calcium carbonate (ACC, 1080 cm^{-1}) are emphasized; (c–g) the Raman mapping of (c) phosphate intensity, (d) ACC/ACP ratio, (e) phosphate peak position and (f) full width at half maximum (FWHM), (g) polarization ratio on the phosphate peak (I-0°/I-90°); (h) schematic representation of the main compositional features of the spike also reporting the underlying predominant fiber arrangement.
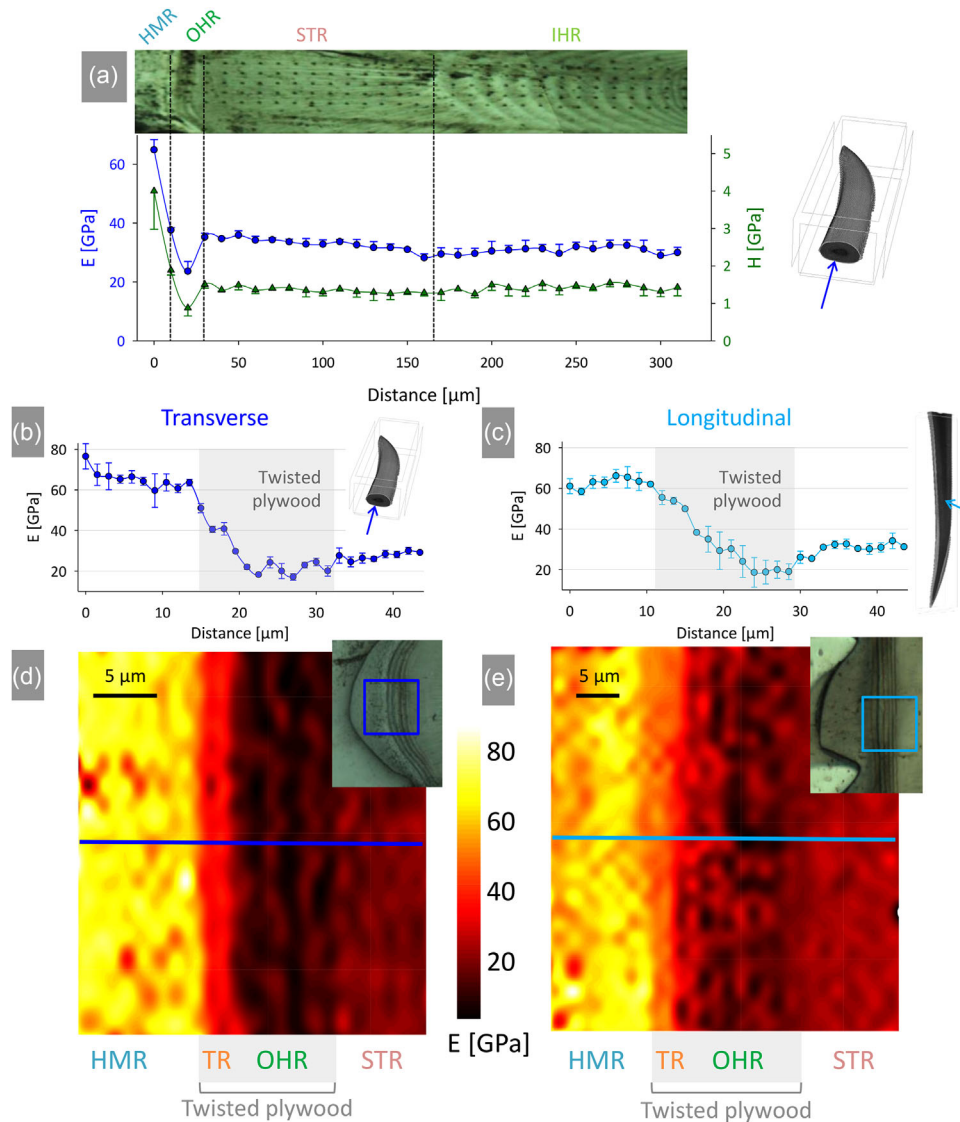
FIGURE 5 Nanomechanical properties of the spike cuticle measured by depth sensing nanoindentation: (a) profile plots of indentation modulus *E* and hardness *H* from the exterior to the interior of the cuticle on a transverse cross section (the nanoindentation grid is visible on the light micrograph). A drop in local mechanical properties within the outer helicoidal region (OHR) is evident; (b and c) spatial variation of indentation modulus measured with higher lateral resolution from the highly mineralized to the striated region, considering both (b) transverse and (c) longitudinal cross sections; (d and e) high-resolution maps of indentation modulus focusing on the transition between the highly mineralized region (HMR) and the STR on (d) transverse and (e) longitudinal cross sections. Probed areas are highlighted in squares on the light micrographs, and the lines indicate the position of the mechanical profiles shown in parts (b) and (c). IHR, inner helicoidal region; STR, striated region; TR, transition region.

the mantis shrimp[42] and the spider fang,[22] a novel feature observed here is that this region, sandwiched between the hard outer cover and the stiff parallel-fiber region, presents substantially lower mechanical properties (modulus and hardness) than the neighborhood.

To further elucidate the possible biomechanical role of the OHR, we performed qualitative fracture experiments: High-load indentation was used to induce cracking, and the sample surface was examined in SEM (Figure 6). Indents placed in the striated region (along the fiber axis, transverse section) require a fairly high load (∼1000 mN) to induce widespread damage: Cracks follow a rather straight path and spread radially in the matrix between fiber stacks (Figure 6a). A central remark

is that all cracks going toward the HMR are stopped by the outer helicoidal arrangement (Figure 6b and Figure S10). This is consistent with the extensive delamination-based damage observed in transverse sections (Figure 2a) and confined within the striated region by the inner and outer twisted plywood. The damage observed in Figure 2a was not induced by indentation but, most likely, by sample preparation. Specifically, sample dehydration and related shrinkage are possible sources of local cracking. Because mineral is believed to replace water, the amount of dehydration (and shrinkage) should be higher in the STR than in the HMR, which is more mineralized and, therefore, should contain less water. At the same time, cracks were not observed in the OHR nor in
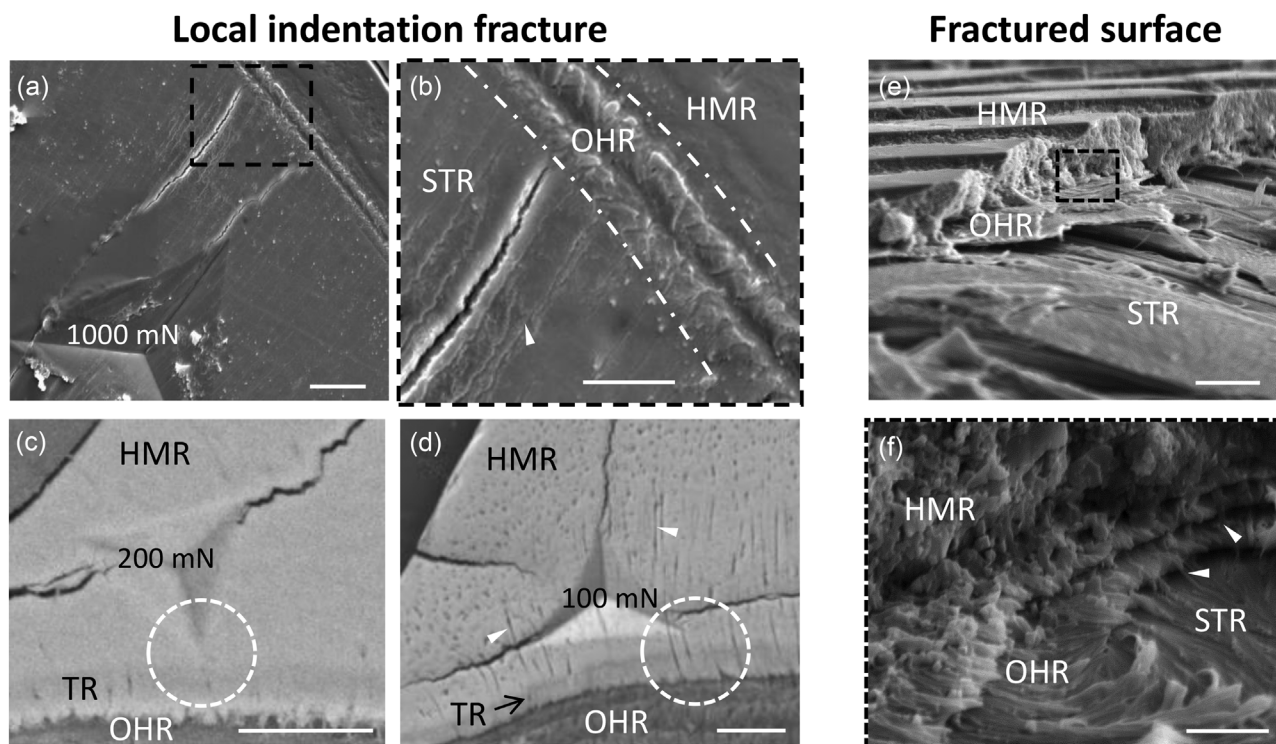
Local indentation fracture

Fractured surface

FIGURE 6 Indentation-induced damage and fracture behavior in the spike cuticle: (a and b) SE-scanning electron microscopy (SEM) images of cracks produced by high-load indentation at 1000 μN in the striated region, which are stopped at the outer helicoidal region as seen both at low (a, scale bar: 20 μm) and high (b, scale bar: 5 μm) magnifications; (c and d) backscattered electron–scanning electron microscopy (BSE–SEM) images of cracks produced by high-load indentation at 200 μN in the highly mineralized region (HMR) observed at low (c, scale bar: 20 μm) and high (d, scale bar: 5 μm) magnifications; (e and f) SE-SEM images of the interface between the HMR and the outer helicoidal region (OHR) in a fractured sample showing the deviation of the fracture plane in correspondence of the OHR (e, scale bar: 10 μm); (f) the presence of vertical chitin–protein fibers belonging to pore canals (arrow heads) and bridging the horizontal fibers beds is highlighted (scale bar: 5 μm). OHR, outer helicoidal region; STR, striated region; TR, transition region.

the IHR, which have a comparable degree of mineralization than the STR but present helicoidal arrangements preventing crack growth. A comparable damage behavior has been reported for the uropod back spike, which has a similar multilayered microstructure, but lacking the external HMR.[42] Indents performed in the HMR require smaller loads (i.e., 50–500 mN) to generate extensive cracking. In this heterogeneous location, a relevant observation is that damage is more likely observed far from the TR, which is also the most compliant zone of the HMR. Indeed, indents placed in the vicinity of this TR either do not cause cracks (Figure 6c) or induce damage running parallel to the TR and its lamella (Figure 6d). Remarkably, no cracks are observed crossing the interface between the HMR and the OHR. Typical high-load indentation curves for the HMR and for the less mineralized but highly anisotropic STR are shown in Figure S11. The HMR featured a characteristic pop-in event (highlighted by the arrow) associated with sudden damage beneath the contact surface. Conversely, the indentation curve of the STR is free from pop-in events, indicating a more progressive damage behavior. The tiny dimension of the OHR (less than 10 μm in width) precluded a quantitative assessment of the fracture toughness as previously done for the impact surface of both spearer and smasher stomatopods.[33,35] Nevertheless, our indentation-based fracture study proves the critical role of the OHR for decoupling damage mechanisms

between the HMR and the STR regions. A closer examination of the surface of a fractured spike highlights the damage behavior from a different perspective (Figure 6e,f). There is a clear transition between the rather straight fractured surface of the HMR and the much rougher surface at its interface with the OHR. Inside the latter, individual lamellae can be seen, suggesting a plausible role in crack deflection and a corresponding switching from a more brittle to a more ductile damage behavior. Furthermore, between the fiber beds of the OHR, unbroken pore canals are present. As in decapods crustaceans,[44] canals of the stomatopods also contain fibers[36] that may act as bridges between the chitin–protein fiber beds, possibly enhancing fracture resistance.[46]

The importance of the thin helicoidal region for the overall damage behavior of the spike is further demonstrated using multimaterial 3D printing (Figure 7). We designed spike-inspired multilayered samples with and without a thin twisted plywood (mimicking the OHR) sandwiched between a stiff monolithic but brittle outer region (mimicking the HMR) and a more compliant but anisotropic parallel-fiber region (mimicking the STR). We used cuboid samples and performed macroscopic penetration tests at high strain rate using a blunt tip (Figure 7a). Notched samples were tested in three-point-bending up to fracture (Figure 7b). The twisted plywood region connecting the still/brittle with the compliant/anisotropic region has a strong impact
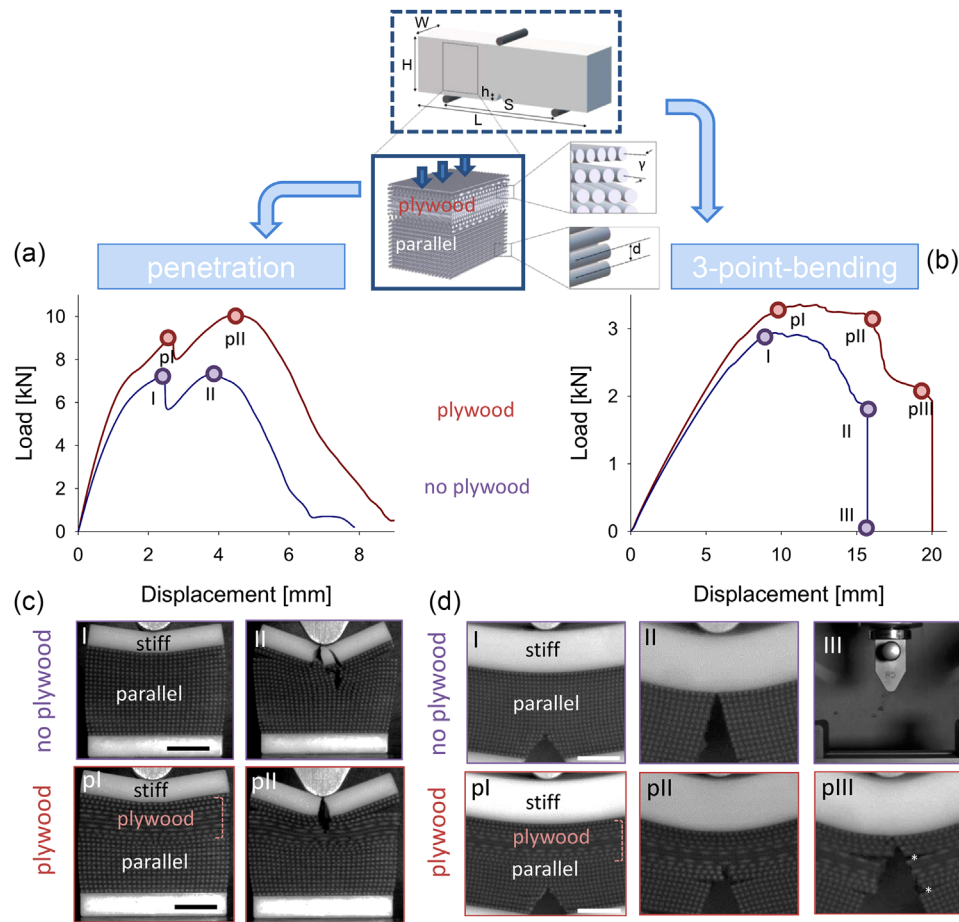
FIGURE 7 Mechanical tests on 3D printed samples mimicking the spike cuticle: (a) blunt penetration and (b) three-point-bending load–displacement curves of samples with and without the plywood connecting the monolithic brittle layer to the parallel-fiber anisotropic region. Snapshots of sample deformation and failure behavior during mechanical testing are given in parts (c) and (d). Scale bars: 1 cm. "*" denotes crack deflection. Details of sample geometry, fiber architecture, and testing configuration are also shown ($H = 4$ cm, $W = 3$ cm, $L = 20$ cm, $h = 1.5$ cm, $s = 16$ cm, $d = 0.1$ cm, the rotation angle between fiber beds γ is 18°).

on the strength, energy absorption, and failure characteristics of the spike-inspired system in both scenarios. Considering penetration tests, force–displacement curves show two peaks (Figure 7a): the first one happening just before the breaking of the stiff outer layer and the second due to damage propagating within the underlying fibrous and more compliant region (Figure 7c). Interestingly, the presence of the plywood not only increases the force needed to propagate the damage in the softer region (by 40%) but also the force necessary to break the stiff layer (by 25%). At the same time, it has no influence on the contact stiffness, as indicated by the same initial slope of the curves. Concerning the three-point-bending tests (Figure 7b), in the sample without the twisted plywood, a main crack nucleates from the notch (Figure 7d-I) and propagates straight in the parallel-fiber region with only minimal delamination (Figure 7d-II). As soon as the crack meets the stiff outer region, a catastrophic failure is observed, and the broken sample "splashes away" from the supports (Figure 7d-III). In the second scenario, the crack also starts from the notch within the parallel-fiber region (Figure 7d-pI) and propagates straight (Figure 7d-pII) up to the

helicoidal region. There, the main crack branches symmetrically into two smaller cracks that propagate horizontally, causing delamination. A similar pattern is repeated one more time, whereas the crack advances in the helicoidal plywood region (Figure 7d-pIII). Crack branching and delamination are important toughening mechanisms that delay catastrophic failure, increasing by almost 50% the energy absorption of the synthetic sample. Interpreting this behavior in the context of the spike may suggest that, although the HMR and the STR are well suited to reinforce the spike under contact forces and axial loading, the combination of these two regions is not efficiently dealing with damage propagation. The thin plywood region may be, therefore, required to fulfill this task.

CONCLUSIONS

The invention of harpoons is a fundamental milestone not only in the evolution of natural life but also for humans.[47] In Nature, evolution

has produced a large variety of harpoons and puncturing devices of increasing complexity, ranging from the passive and fairly simple cacti spines,[48] to the more sophisticated offensive tools, such as spider[41] and viper fangs,[49] scorpion stinger,[50] and even, including drilling machines as in mosquito or parasitic wasps.[51,52] Particularly fascinating are the chitinous penetrating tools of arthropods, which often allow piercing through several layers of a similar material, and possessing multiple modifications to fulfill such task.[53] The spikes emerging from the spearing appendage of the mantis shrimps are biological harpoons deployed very quickly to impale and grab moving fishes that have the bad luck to swim nearby. This is a challenging task requiring the ability not only to resist the initial impact with the scaly skin of the prey but also to penetrate it for several millimeters to avoid the fish swimming away. Here, we have investigated the spike using imaging and material characterization techniques, to elucidate the many design strategies of this biological tool. From the material point of view, the spike cuticle of stomatopods is a chitin-based multilayered biocomposite, reinforced by different minerals together with compositional gradients and specific fiber arrangement.[36] A hard heavily mineralized outer shell of crystalline FAP, essentially lacking fibers, is designed to resist impact and wear. This exterior cover is combined with inner fiber-rich regions characterized by lower mineral content and amorphous minerals (ACP and ACC). Two distinct fiber architectures are observed: a unidirectional arrangement bordered by helicoidal twisted plywood of dissimilar size. The latter is ubiquitous in arthropod[12] and presents two main biomechanical advantages[22]: Starting from a strongly anisotropic elementary building block (the chitin–protein fiber), it provides the cuticle with in-plane isotropic mechanical behavior and high shear stiffness.[41,54] Moreover, the helicoidal twisted plywood arrangement has a remarkable fracture resistance obtained by interacting with cracking at different levels,[55] essentially enhancing crack driving force[56] and reducing strain energy release rate.[57] Conversely, the parallel-fiber organization is less usual[22] and it is used here, with fibers well oriented along the long axis of the spike from the tip to the base, to enhance stiffness and bending resistance. The combination of parallel fibers with a twisted plywood region is therefore well suited to support a complex mechanical environment with axial, bending, and torsional loading. A central finding of our work is that, in the spike cuticle, the parallel-fiber region is "joined" to the highly mineralized cover by a thin fiber-rich twisted plywood region, showing compositional modifications that make it the most compliant zone of the entire spike. In the cuticle, plywood (or Bouligand) structures are generally thick regions occupying a major part of the cuticle width and previous works have demonstrated their superior fracture toughness.[34,58,59] The unique feature observed here is the presence of an extremely thin plywood structure (i.e., less than 10 μm in width) sandwiched between two very dissimilar regions and allowing the integration of a highly mineralized brittle outer layer with a less mineralized but highly anisotropic straight fibers region. Not only the plywood is very effective to stop crack propagation (both from the striated region to the hard shell and vice versa), as demonstrated by nanoindentation fracture experiment and by three-point-bending tests on spike-inspired synthetic systems, but it also increases the force required to penetrate both the stiff layer and the underlying complaint fibrous matrix (as assessed on 3D printed replicas). Considering the attachment of different materials, introducing a more compliant region at the interface joining two dissimilar components is a construction principle common to other biological systems.[60] Tendon, for example, attaches to bone through a transition zone which is not only more compliant than bone but also than tendon.[61] This region, which co-localizes with the unraveling and splaying out of tendon fibers into smaller fibrils[60] and which is made up of fibrocartilage,[62] is believed to protect the attachment region by reducing stress concentration, effectively strengthening the interface.[63] In analogy with the tendon–bone attachment, the thin and more compliant twisted plywood region may offer protection against stress localization at the transition between the hard and the parallel-fiber region, hence increasing the damage tolerance of the spike. Helix-reinforced composites are common in engineering applications and the construction principles of biological materials can improve the performance of the synthetic counterparts.[64] Focusing on the mantis shrimp dactyl club, Bouligand and herringbone arrangements, as well as nanoscale features of the impact surface, have inspired the design of impact resistance man-made composites.[65] In the light of the endless advancement in nano- and microscale manufacturing methods, the biological tool investigated here could inspire the design of new synthetic harpoons, for example, based on environmentally friendly and recyclable building units as seen in the spike cuticle, with improved wear resistance and puncture abilities for repeated piercing on different surfaces.

EXPERIMENTAL SECTION

Stomatopods and sample preparation

The specie of spearing mantis shrimps used in this study is *L. maculata* (Fabritius, 1793) also called the striped mantis shrimp (Figure 1a). Eight living stomatopods from Kendari (Indonesia), ranging from 20 to 40 cm in length, were delivered by Marine Life (Paris, France) and were kept in captivity in proper tanks at the Functional Morphology Lab (University of Liège). Spikes were harvested from three different individuals after euthanasia, for a total of nine spikes analyzed with different methods. All specimens were dissected in the intermolt stage C4, corresponding to entire and mature cuticle.[66] Distal spikes were then separated from each other (Figure 1b). Samples imaged with micro-CT ($n = 2$) were directly embedded in epoxy resin to minimize movement artifacts. Samples used for SEM ($n = 4$), Raman ($n = 3$), and nanoindentation ($n = 6$) were dehydrated in a graded series of ethanol bath (50%, 70%, 90%, and 100%) and embedded in epoxy resin (EpoFix resin Kit, Struers Inc., Germany) under vacuum. The resin blocks were then polished (Rotopol-2, Struers, Germany) with a series of silicon carbide disks of decreasing grain size (P800, P1200, P2400, P4000, Matador, Germany). Final polishing steps were performed with a diamond spray (DP-Spray P 1 μm, Struers, Germany) and an aluminum suspension (Eposil F, 0.1 μm, ATM, Germany).

Micro-CT imaging and processing

Micro-CT scans of resin-embedded spikes were done at a nominal isotropic voxel size of 2 μm. The micro-CT (SkyScan 1272, Bruker, Belgium) was operated at a tube voltage of 60 kV and current of 166 μA, in combination with a 0.25 mm thick aluminum filter. The samples were rotated over 180° with a rotation step of 0.2° (corresponding to 940 projections), with an exposure time of 3600 ms and a frame averaging of 4, leading to a scan time of approximately 4 h. A bigger sample, including also the dactyl, was scanned at a lower resolution of 15 μm. Scans were reconstructed using Nrecon (v.1.7.5.2, Skyscan) and further analyzed with the software ImageJ (v.1.52a), Matlab (R2018a; The MathWorks, USA), and CTAn (v.1.19.4.0, Skyscan). Each virtual spike was first aligned along its principal axes of inertia using BoneJ (v.1.4.3),[67] a module of ImageJ. Images were binarized using a global threshold based on Otsu's method[68] and filtered to extract the biggest connected component. Geometrical properties of the cross sections were measured using the Matlab Image Processing Toolbox. Using the general formula $I = \int z^2 dA$, where z is the shortest distance of the area element dA from a given axis, the planar (I_x and I_y) and polar ($J = I_x + I_y$) second moments of area passing through the centroid were computed. Major and minor axes were deduced by fitting an ellipse having the same second moments of area as the current cross section. Eccentricity was computed as the ratio of the distance between the foci of the ellipse and the length of its major axis. Principal moments of area about the minor (I_{min}) and the major (I_{max}) axis of each cross section, corresponding approximately to dorsoventral and lateral loadings, were calculated based on Mohr's circle theory. To compute the curvature κ of the spike, first a centroid profile line was extracted smoothed and down-sampled, to reduce the noise. At each location along the profile line, the local radius of curvature was computed by fitting circles, always considering three neighboring points. The curvature vector was obtained by dividing the unit vector pointing from the middle point of the triplet to the center of the circle by the radius of curvature.[69] A similar procedure was followed to compute the radius of curvature at the tip.

Scanning electron microscopy and energy-dispersive spectroscopy

Observations of polished sections were carried out with an environmental scanning microscope ESEM-FEG XL-30 (FEI, The Netherland) in low vacuum mode (0.4 Torr) at 20 KeV accelerating voltage. Images were taken using a backscattered electron detector. A silicon drift detector of X-rays (Bruker, USA) with a super-ultrathin window was used to obtain energy-dispersive spectra and to perform elemental mapping using a QUANTAX analyzer and the software Esprit 2.1 (Bruker, USA). To measure the different element concentrations, the following energy peaks were used: carbon K_α peak (0.277 keV), phosphorus K_α peak (2.013 keV), calcium K_α peak (3.690 keV), magnesium K_α peak (1.253 keV), fluorine K_α peak (0.677 keV), and Sodium K_α peak (1.041 keV). Fractured samples were sputter-coated with silver (SCD030, Balzers, Liechtenstein) and observed in high vacuum mode using the same microscope with an acceleration voltage of 15 kV and a secondary electron detector. Measurements of grooves and serrations were made using the software ImageJ[70] on SEM–BSE micrographs of the spike in longitudinal and transversal sections to quantify their length and depth.

Raman spectroscopy

Polished sections of the spike were analyzed by Raman spectroscopy with a green DPSS laser ($\lambda = 532$ nm, LabRAM 300, HORIBA Jobin Yvon, Japan). Spectra were acquired along straight lines at several different positions within the HMR, the outer helicoidal layer, and the striated region of the cuticle. Each spectrum was acquired for 5 s. High-resolution Raman mapping was performed on the outer region of the spike cuticle with the same microscope by focusing the laser beam through an Olympus MLPlan objective (NA 0.75), using an integration time of 1 s and resulting in a nominal pixel size of 500 nm. The mapping was performed with two different polarization angles (0° and 90°). The obtained spectra were analyzed with RStudio (RStudio Team, 2015) to extract the phosphate intensity (peak intensity in the 952–968 cm^{-1} region), the carbonate intensity (peak intensity in the 1077–1083 cm^{-1} region), the phosphate position (wavelength at which the phosphate $\upsilon1$ vibration mode is the highest), the FWHM (width of the phosphate $\upsilon1$ vibration mode at its half height), and the polarization ratio (intensity of the 960 cm^{-1} band in 0°/90° polarization).

Depth sensing nanoindentation

Nanoindentation tests were conducted with a TriboIndenter TI950 (Bruker, USA) on repolished surface (the same samples used for SEM were probed), considering both transversal and longitudinal sections. We first used a Berkovich diamond tip to perform nanoindentation grids spanning across the different regions of the spike with indents spaced 10 μm apart (grid size in Figure 5a: 32 × 5 indents). We employed a trapezoidal load-controlled function (10–5–10 s for loading, holding, and unloading segments) with a peak load of 5000 μN. Higher resolution nanoindentation mapping covering ~45 × 45 μm areas was carried out on two locations at the interface between the HMR and the OHR after scanning the surfaces with the tip of the indenter to check the roughness (average RMS roughness in the range ~16–25 nm depending on the location). We used a sharper cube corner probe and a displacement-controlled indentation (10–5–10 s) with a maximum penetration depth of 200 nm, allowing a smaller spacing of 1.5 μm between indents.[71] Both tips were calibrated in fused quartz. Force–depth curves were analyzed with the Oliver–Pharr method[72] to extract the indentation modulus E and hardness H. High lateral resolution nanoindentation data were used to generate 2D maps of the indentation modulus (Figure 5d,e and Figure S8) and raw data were interpolated with the MESHGRID function of Matlab. A qualitative fracture study was performed on polished samples with a high load

(10 N) transducer (OmniProbe, Bruker, USA) equipped with a Berkovich probe. Several indentation loads ranging from 50 to 1000 mN were done to generate surface damage in different locations of the spike.

3D printing and testing

Spike-inspired samples were designed with IronCAD (2020, USA), fabricated using a 3D multimaterial polyjet printer (Objet260, Stratasys, USA), and tested. Specifically, we performed penetration tests with a blunt tip (5 mm tip radius) and three-point-bending tests (MTS Criterion C43.304, USA). For the penetration tests, we considered cuboid samples having the following dimensions: 4 cm × 3 cm × 3 cm (height, width, and length). For the three-point-bending tests, we fabricated beam-shaped samples, with dimensions: height (H) 4 cm, width (W) 3 cm, and length (L) 20 cm. Each sample was a multilayer composite, featuring an outer monolithic region (mimicking the heavily mineralized shell) and an inner fiber-reinforced region. For the fiber-reinforced part, two different architectures were considered: (i) a thick region composed of unidirectional parallel fibers, all oriented perpendicular to the longitudinal axis of the sample (mimicking the striated region) and (ii) a two-layer system with a thin helicoidal twisted plywood region (mimicking the OHR) sandwiched between the monolithic part and the unidirectional fibers array. The monolithic layer as well as the fibers were printed with a rigid glassy polymer (commercial name Vero White Plus), having Young's modulus at room temperature in the range of 2–3 GPa.[73] For the matrix embedding, the fibers we used a rubbery polymer (commercial name Tango Black Plus) with a tangent modulus at room temperature of about 0.5–1 MPa.[74] Based on the printer resolution and considering the finite size (i.e., up to 150 μm) and the properties of the interface between fiber and matrix,[75] the 3D printed fibers had a diameter of 600 μm. For the region mimicking the helicoidal structure, 10 sheets were stacked with a pitch angle of 18°. At the bottom surface of the samples, a rigid layer made up of Vero White Plus was added to prevent excessive sink-in at the contact point with the supports. A notch (0.15 cm deep) was directly printed in the samples to trigger damage initiation within the parallel fiber array. Penetration tests were done at 10 mm/min, whereas three-point-bending tests (span length of 16 cm) were conducted at 60 mm/min, considering preload of 5 N and with a 30 kN load cell. During tests, samples were imaged with an HD camera at 15 fps, and movies were used to analyze deformation mechanisms. Mechanical tests were performed 1 day after printing to have always the same post-curing time. Fabrication, storage, and testing were done in a room with controlled humidity and temperature to minimize experimental variability.

AUTHOR CONTRIBUTIONS

Conceptualization; data curation; formal analysis; funding acquisition; investigation; methodology; software; validation; visualization; writing – original draft; writing –review and editing: Yann Delaunois. *Formal analysis; investigation; methodology; software; visualization; writing – original draft; writing – review and editing*: Alexandra Tits and Quentin Grossman. *Formal analysis; investigation; methodology; writing – original draft; writing – review and editing*: Sarah Smeets. *Formal analysis; investigation; methodology; resources; software; supervision; validation; visualization; writing – original draft; writing – review & editing*: Cedric Malherbe. *Methodology; resources; supervision; validation; writing – original draft; writing – review and editing*: Gauthier Eppe. *Methodology; resources; software; supervision; validation; writing – original draft; writing – review and editing*: Harry van Lenthe. *Conceptualization; data curation; formal analysis; funding acquisition; investigation; methodology; project administration; resources; software; supervision; validation; visualization; writing – original draft; writing – review and editing*: Davide Ruffoni. *Conceptualization; data curation; formal analysis; funding acquisition; investigation; methodology; project administration; resources; software; supervision; validation; visualization; writing – original draft; Writing – review & editing*: Philippe Compere.

CONFLICT OF INTEREST STATEMENT

The authors declare no conflict of interests.

ETHICS STATEMENT

The authors confirm that they have followed the ethical policies of the journal.

DATA AVAILABILITY STATEMENT

Data available upon reasonable requests.

ORCID

Alexandra Tits https://orcid.org/0000-0002-2871-2785
G. Harry van Lenthe https://orcid.org/0000-0001-8303-4959
Davide Ruffoni https://orcid.org/0000-0003-3714-7594

PEER REVIEW

The peer review history for this article is available at https://publons.com/publon/10.1002/ntls.20220060.

REFERENCES

1. Wainwright SA, Gosline JM, Biggs WD, Currey JD. *Mechanical Desing in Organisms.* Princeton University Press; 1982.
2. Hunger T, Steinbrecht RA. Functional morphology of a double-walled multiporous olfactory sensillum: the sensillum coeloconicum of *Bombyx mori* (Insecta, Lepidoptera). *Tissue Cell.* 1998;30:14.
3. Boxshall Ga. The evolution of arthropod limbs. *Biol Rev Camb Philos Soc.* 2004;79:253.
4. Fratzl P, Barth FG. Biomaterial systems for mechanosensing and actuation. *Nature.* 2009;462:442.
5. Gorb S. *Attachment Devices of Insect Cuticle.* Kluwer Academic Publishers; 2001.

6. Dirks JH, Parle E, Taylor D. Fatigue of insect cuticle. *J Exp Biol.* 2013;216:1924.

7. Bentov S, Zaslansky P, Al-Sawalmih A, et al. Enamel-like apatite crown covering amorphous mineral in a crayfish mandible. *Nat Commun.* 2012;3:839.

8. Taylor JRA, Patek SN. Ritualized fighting and biological armor: the impact mechanics of the mantis shrimp's telson. *J Exp Biol.* 2010;213:3496.

9. Yaraghi NA, Trikanad AA, Restrepo D, et al. Multiscale biological composites: the Stomatopod Telson: convergent evolution in the development of a biological shield (Adv. Funct. Mater. 34/2019). *Adv Funct Mater.* 2019;29:1970232.

10. Agez G, Bayon C, Mitov M. Multiwavelength micromirrors in the cuticle of scarab beetle *Chrysina gloriosa. Acta Biomater.* 2017;48:357.

11. Anderson PSL. Making a point: shared mechanics underlying the diversity of biological puncture. *J Exp Biol.* 2018;221:1-12.

12. Neville AC. *Biol. Integument.* Springer Berlin Heidelberg; 1984:611-625.

13. Compère P, Jeuniaux C, Goffinet G. In: Forest J, von Vaupel Klein J C, Schram F R, eds. *Crustac. Revis. Updat. from Trait Zool.* Koninklijke Brill; 2004:59-144.

14. Fabritius HO, Sachs C, Raabe D, Nikolov S, Friák M, Neugebauer J. *Chitin, Topics in Geobiology.* 2011:36-58.

15. Raabe D, Romano P, Sachs C, et al. Microstructure and crystallographic texture of the chitin-protein network in the biological composite material of the exoskeleton of the lobster *Homarus americanus. Mater Sci Eng.* 2006;421:143.

16. Belamie E, Mosser G, Gobeaux F, Giraud-Guille MM. Possible transient liquid crystal phase during the laying out of connective tissues: α-chitin and collagen as models. *J Phys Condens Matter.* 2006;18:S115.

17. Politi Y, Bar-On B, Fabritius HO. Mechanics of arthropod cuticle-versatility by structural and compositional variation. *Springer Ser Mater Sci.* 2019;282:287.

18. Rudall KM, Kenchington W. The chitin system biol. *Rev Camb Philos Soc.* 1973;48:597.

19. Horst MN, Freeman JA. *Crustacean Integument.* CRC Press; 1993.

20. Compère P, Jeuniaux C, Goffinet G. In: Forest J, von Vaupel Klein J C, eds. *Crustac. Revis. Updat. from Trait. Zool.* 2004:44-118.

21. Cribb BW, Stewart A, Huang H, et al. Insect mandibles-comparative mechanical properties and links with metal incorporation. *Naturwissenschaften.* 2008;95:17.

22. Politi Y, Priewasser M, Pippel E, et al. A spider's fang: how to design an injection needle using chitin-based composite material. *Adv Funct Mater.* 2012;22:2519.

23. Giraud-Guille MM. Fine structure of the chitin-protein system in the crab cuticle. *Tissue Cell.* 1984;16:75.

24. Fabritius HO, Ziegler A, Friák M, et al. Functional adaptation of crustacean exoskeletal elements through structural and compositional diversity: a combined experimental and theoretical study. *Bioinspir Biomim.* 2016;11(5):055006. 10.1088/1748-3190/11/5/055006

25. Chen P, Lin A, Lin Y, et al. Structure and mechanical properties of selected biological materials. *J Mech Behav Biomed Mater.* 2008;1(3):208-226.

26. Van Der Wal C, Ahyong ST, Ho SYW, Lo N. The evolutionary history of Stomatopoda (Crustacea: Malacostraca) inferred from molecular data. *PeerJ.* 2017;5:1-17.

27. Haug JT, Haug C, Maas A, Kutschera V, Waloszek D. Evolution of mantis shrimps (Stomatopoda, Malacostraca) in the light of new Mesozoic fossils. *BMC Evol Biol.* 2010;10:290.

28. Grunenfelder LK, Milliron G, Herrera S, et al. Ecologically driven ultrastructural and hydrodynamic designs in stomatopod cuticles. *Adv Mater.* 2018;30:1705295.

29. Tadayon M, Amini S, Masic A, Miserez A. The mantis shrimp saddle: a biological spring combining stiffness and flexibility. *Adv Funct Mater.* 2015;25:6437.

30. Anderson PSL, Claverie T, Patek SN. Levers and linkages: mechanical trade-offs in a power-amplified system. *Evolution (NY).* 2014;68:1919.

31. deVries MS, Murphy EAK, Patek SN. Strike mechanics of an ambush predator: the spearing mantis shrimp. *J Exp Biol.* 2012;215:4374.

32. Weaver JC, Milliron GW, Miserez A, et al. The stomatopod dactyl club: a formidable damage-tolerant biological hammer. *Science.* 2012;336(6086):1275-1280.

33. Amini S, Tadayon M, Idapalapati S, Miserez A. The role of quasi-plasticity in the extreme contact damage tolerance of the stomatopod dactyl club. *Nat Mater.* 2015;14:943.

34. Yaraghi NA, Guarin-Zapata N, Grunenfelder LK, et al. A sinusoidally architected helicoidal biocomposite. *Adv Mater.* 2016;28(32):6835.

35. Amini S, Masic A, Bertinetti L, et al. Textured fluorapatite bonded to calcium sulphate strengthen stomatopod raptorial appendages. *Nat Commun.* 2014;5(1):3187.

36. Delaunois Y, Smeets S, Malherbe C, et al. Structure and mineralization of the spearing mantis shrimp (Stomatopoda; *Lysiosquillina* maculata) body and spike cuticles. *J Struct Biol.* 2021;213:107810.

37. Schulz JR, Norton AG, Gilly WF. The projectile tooth of a fish-hunting cone snail: conus catus injects venom into fish prey using a high-speed ballistic mechanism. *Biol Bull.* 2004;207:77.

38. Wu J, Yan S, Zhao J, Ye Y. Barbs facilitate the helical penetration of honeybee (*Apis mellifera ligustica*) stingers. *PLoS One.* 2014;9:e103823.

39. Ramasubramanian MK, Barham OM, Swaminathan V. Mechanics of a mosquito bite with applications to microneedle design. *Bioinspir Biomim.* 2008;3:046001.

40. Vittori M, Srot V, Žagar K, et al. Axially aligned organic fibers and amorphous calcium phosphate form the claws of a terrestrial isopod (Crustacea). *J Struct Biol.* 2016;195:227.

41. Bar-On B, Barth FG, Fratzl P, Politi Y. Multiscale structural gradients enhance the biomechanical functionality of the spider fang. *Nat Commun.* 2014;5:2041.

42. Li S, Liu P, Lin W, et al. Optimized hierarchical structure and chemical gradients promote the biomechanical functions of the spike of mantis shrimps. *ACS Appl Mater Interfaces.* 2021;13(15):17380-17391. 10.1021/acsami.1c02867

43. Meyers MA, Chen P-Y, Yu-Min Lin A, Seki Y. Biological materials: structure and mechanical properties. *Prog Mater Sci.* 2008;53:1.

44. Compère P, Goffinet G. Ultrastructural shape and three-dimensional organization of the intracuticular canal systems in the mineralized cuticle of the green crab *Carcinus maenas. Tissue Cell.* 1987;19:839.

45. Leroy G, Leroy N, Penel G, Rey C, Lafforgue P, Bres E. Polarized micro-raman study of fluorapatite single crystals. *Appl Spectrosc.* 2000;54:1521.

46. Huang W, Restrepo D, Jung JY, et al. Multiscale toughening mechanisms in biological materials and bioinspired designs. *Adv Mater.* 2019;31(43):1901561.

47. Hughes SS. Getting to the point: evolutionary change in prehistoric weaponry. *J Archaeol Method Theory.* 1998;5:345.

48. Crofts SB, Anderson PSL. The influence of cactus spine surface structure on puncture performance and anchoring ability is tuned for ecology. *Proc R Soc B Biol Sci.* 2018;21:285. 10.1098/rspb.2018.2280

49. Crofts SB, Lai Y, Hu Y, Anderson PSL. How do morphological sharpness measures relate to puncture performance in viperid snake fangs? *Biol Lett.* 2019;15:20180905.

50. Zhao ZL, Shu T, Feng XQ. Study of biomechanical, anatomical, and physiological properties of scorpion stingers for developing biomimetic materials. *Mater Sci Eng C.* 2016;58:1112.

51. Cerkvenik U, van de Straat B, Gussekloo SWS, van Leeuwen JL. Mechanisms of ovipositor insertion and steering of a parasitic wasp. *Proc Natl Acad Sci.* 2017;114:E7822.

52. Kong XQ, Wu CW. Measurement and prediction of insertion force for the mosquito fascicle penetrating into human skin. *J Bionic Eng.* 2009;6:143.

53. Politi Y, Bertinetti L, Fratzl P, Barth FG. The spider cuticle: a remarkable material toolbox for functional diversity. *Philos Trans R Soc A: Math Phys Eng Sci.* 2021;379:20200332. 10.1098/rsta.2020.0332

54. Nikolov S, Petrov M, Lymperakis L, et al. Revealing the design principles of high-performance biological composites using ab initio and multiscale simulations: the example of lobster cuticle. *Adv Mater.* 2010;22:519.

55. Suksangpanya N, Yaraghi NA, Pipes RB, Kisailus D, Zavattieri P. Crack twisting and toughening strategies in Bouligand architectures. *Int J Solids Struct.* 2018;150:83.

56. Fischer FD, Kolednik O, Predan J, Razi H, Fratzl P. Crack driving force in twisted plywood structures. *Acta Biomater.* 2017;55:349.

57. Suksangpanya N, Yaraghi NA, Kisailus D, Zavattieri P. Twisting cracks in Bouligand structures. *J Mech Behav Biomed Mater.* 2017;76:38.

58. Yin S, Chen H, Yang R, et al. Tough nature-inspired helicoidal composites with printing-induced voids. *Cell Rep Phys Sci.* 2020;1:100109.

59. Wu K, Song Z, Zhang S, et al. Discontinuous fibrous Bouligand architecture enabling formidable fracture resistance with crack orientation insensitivity. *Proc Natl Acad Sci USA.* 2020;117:15465.

60. Rossetti L, Kuntz LA, Kunold E, et al. The microstructure and micromechanics of the tendon-bone insertion. *Nat Mater.* 2017;16(6):664-670.

61. Tits A, Ruffoni D. Joining soft tissues to bone: insights from modeling and simulations. *Bone Rep.* 2021;14:100742.

62. Tits A, Plougonven E, Blouin S, et al. Local anisotropy in mineralized fibrocartilage and subchondral bone beneath the tendon-bone interface. *Sci Rep.* 2021;11:1. 2021 111.

63. Liu YX, Thomopoulos S, Birman V, Li JS, Genin GM. Bi-material attachment through a compliant interfacial system at the tendon-to-bone insertion site. *Mech Mater.* 2012;44:83.

64. Zorzetto L, Ruffoni D, Zorzetto L, Ruffoni D. Wood-inspired 3D-printed helical composites with tunable and enhanced mechanical performance. *Adv Funct Mater.* 2019;29:1805888.

65. Behera RP, Le Ferrand H. Impact-resistant materials inspired by the mantis shrimp's dactyl club. *Matter.* 2021;4:2831.

66. Reaka ML. Molting in stomatopod crustaceans. I. Stages of the molt cycle, setagenesis, and morphology. *J Morphol.* 1975;146:55.

67. Doube M, Klosowski MM, Arganda-Carreras I. BoneJ: free and extensible bone image analysis in ImageJ. *Bone.* 2010;47:1076.

68. Otsu N. A threshold selection method from gray-level histograms. *IEEE Trans Syst Man Cybern.* 1979;9(1):62-66.

69. Mjaavatten A. MATLAB Cent. File Exch. 2022.

70. Schneider CA, Rasband WS, Eliceiri KW. NIH Image to ImageJ: 25 years of image analysis. *Nat Methods.* 2012;9:671. 2012 97.

71. Sachs C, Fabritius H, Raabe D. Hardness and elastic properties of dehydrated cuticle from the lobster *Homarus americanus* obtained by nanoindentation. *J Mater Res.* 2006;21:1987.

72. Oliver WC, Pharr GM. An improved technique for determining hardness and elastic modulus using load and displacement sensing indentation experiments. *J Mater Res.* 1992;7:1564.

73. Lumpe TS, Mueller J, Shea K. Tensile properties of multi-material interfaces in 3D printed parts. *Mater Des.* 2019;162:1.

74. Slesarenko V, Rudykh S. Towards mechanical characterization of soft digital materials for multimaterial 3D-printing. *Int J Eng Sci.* 2018;123:62.

75. Zorzetto L, Andena L, Briatico-Vangosa F. Properties and role of interfaces in multimaterial 3D printed composites. *Sci Rep.* 2020;10:1.

SUPPORTING INFORMATION

Additional supporting information can be found online in the Supporting Information section at the end of this article.